



First-principles modeling of conductivity at the (001), (110), and (111) SrTiO₃/LaAlO₃ heterointerfaces

David G. Gonzalez , Gaoxue Wang , Ping Yang ,* and Enrique R. Batista [†]
Theoretical Division, Los Alamos National Laboratory, Los Alamos, New Mexico 87545, USA

 (Received 1 February 2021; revised 29 July 2021; accepted 29 September 2021; published 14 October 2021)

The complex polar oxide heterojunction of SrTiO₃/LaAlO₃ (STO/LAO) is of great interest due to the emergent physical phenomena observed at the interface. STO and LAO separately are wide band-gap insulators. However, upon joining them at the 001, 110, and 111 crystallographic planes, the interface undergoes a transition to a conductive state. Although first-principles modeling of the 001 plane interface has been widely studied, there is a lack of reports regarding the 110 and 111. This paper expands the theoretical model of the STO/LAO heterointerface to the three crystallographic planes (001, 110, and 111) where the conductivity has been experimentally reported. The calculations showed that whereas at the 001 interface the conductivity appears at a critical thickness of 4 monolayers of LAO, the 110 and 111 planes have no clear critical thickness; these two interfaces were always conductive. Nevertheless, the number of conductive electrons per unit cell increases with the thickness of the LAO layer in the 110 and 111 interfaces. This is related to the energy levels downshifting due to the electrostatic potential buildup (which was in the opposite direction respect to the 001 interface), increasing the number of conductive states below the Fermi level. Given the absence of a critical thickness and the fact that chemical intermixing and oxygen vacancies at the interface were not considered, the main mechanism responsible for the conductivity in the 110 and 111 planes was attributed to the large structure reconstruction that locally changes the energy levels at the interface causing charge transfer and accumulation at the layers close to the interface.

DOI: [10.1103/PhysRevB.104.155306](https://doi.org/10.1103/PhysRevB.104.155306)

I. INTRODUCTION

Heterointerfaces between materials with different polarity have been widely studied due to the observation of unexpected and interesting emergent properties not present in the individual components [1,2]. The polar discontinuity together with the lattice mismatch induce a mixture of ionic and electronic reconstruction close to the interface, which are the main contributors behind the emergent phenomena. These devices can be made of different elements and thickness allowing fine-tuning of the heterojunction, obtaining a wide variety of properties that range from insulator to superconductor. A practical application of these principles is found in current oxide thin-film technology and are also of main interest in the development of novel electronic devices [3]. An example of such polar oxide heterointerface is the one between strontium titanate (STO) and lanthanum aluminate (LAO). Both wide band-gap insulators, when epitaxially joined a 2D high electron mobility at the interface of STO/LAO has been measured. An interesting feature of the STO/LAO system is that the 2D conductivity suddenly increases by several orders of magnitude when the LAO layer is at a critical thickness of 4, 7, and 9 mono layers at the 001, 110, and 111 interfaces, respectively [4,5]. The conductive behavior in addition with 2D

superconductivity and ferromagnetism has also been reported [6–10].

There are four proposed mechanisms that may contribute to the 2D metallic behavior in STO/LAO interface: polar discontinuity [4,11], structural reconstruction [12], chemical intermixing [11,13], and oxygen vacancies [14]. Due to the different polar nature of the materials, polar discontinuities result in asymmetrical buildup of electrostatic potential along the direction perpendicular to the interface. As is the case for STO/LAO at the 001 plane, STO is neutral whereas LAO is polar. At the critical thickness the electrostatic potential buildup causes the energy of the valence states in the LAO outer layers to rise above the Fermi level. The electrons on this level tunnel to the nearby STO, giving rise to metal-induced gap states that are very localized at the interface [15]. A schematic of this process is shown in Fig. 1. Structural reconstruction of the nearby layers close to the interface is the result of the lattice mismatch between the two materials. LAO and STO have a lattice mismatch of 2.8%, resulting in a strain-induced structural reconstruction which locally changes the band structure and increases the carrier density. The chemical intermixing effect is the result of the interfaces not being atomically sharp. Depending on the growth conditions the stoichiometry at the interface can change due to intermixing of lanthanum and strontium species effectively creating an alloy. Due to its similar atomic radius and electronegativity, lanthanum (La⁺³) is a good donor dopant for STO, replacing strontium (Sr⁺²) making it *n*-type conductive [16]. Finally, lattice defects in the STO/LAO structure in the form of oxygen

*pyang@lanl.gov

[†]erb@lanl.gov

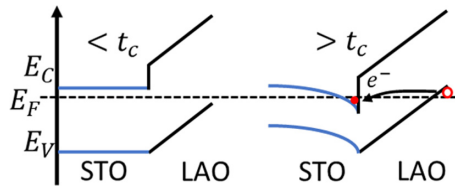


FIG. 1. Energy bands diagram of the electronic reconstruction due to the polar discontinuity at 001 when the thickness of LAO is smaller (left) and larger (right) than the critical thickness (t_c).

vacancies can dope the STO interface increasing the carrier density.

Theoretical modeling of STO/LAO has been a vital tool in the studying of this system. In general, there are two main approaches in the simulation of the STO/LAO interface: a superlattice or a slab. The superlattice cell is composed of continuous interlacing stacks of STO and LAO, while the slab model is composed of a STO/LAO supercell separated by a vacuum layer. Lee and Demkov [11] simulated the critical thickness of 001 STO/LAO interface using a symmetric slab supercell. They showed more evidence in favor of the electronic reconstruction scenario previously proposed by Ohtomo and Hwang [4]. Janika *et al.* [10,15] used the superlattice model to study the magnetic and electron confinement at 001 STO/LAO interface. They were able to replicate the conductivity at the TiO_2 -terminated 001 STO/LAO interface, and also found that for thinner STO layers the system should be magnetic. Additional evidence in favor of the electronic reconstruction was also shown by Pentcheva and Pickett [17,18]. They used an asymmetric slab supercell, and also demonstrated the importance of a proper ionic relaxation using a slab system to obtain the critical thickness at the 001 interface. Guan *et al.* [19] made a comparison between the superlattice and slab models at the 001 interface, showing the general picture that the superlattice is capable of simulating the conductivity but, to obtain the insulator to metal transition, a slab model is needed. Annadi *et al.* [20] study the anisotropy of the two-dimension electron gas formed at the 110 STO/LAO interface (observed experimentally by them) using a symmetric slab supercell. Beltrán and Muñoz [21] used a superlattice to show that for the 111 STO/LAO interface there should exist correlated-electron ground states that depend on the STO layer thickness, which yields different behaviors from nonmagnetic metal to antiferromagnetic Mott insulator. The vast majority of these first-principles studies has been focused at the interface along the 001 plane; this paper further expands those studies to the 110 and 111 planes, giving an overall comparison of the metallic behavior of STO/LAO interface on all three crystallographic planes. See Refs. [22–25].

II. LAO AND STO PROPERTIES

LAO (LaAlO_3) and STO (SrTiO_3) are wide band-gap ceramic oxides with a perovskite crystalline structure (ABO_3); their simple-cubic unit cell is shown in Fig. 2. At room temperature LAO has a rhombohedral unit cell which changes to simple cubic at about 815 K. The cubic to rhombohedral distortion is very small (0.087° at 300 K); therefore, LAO

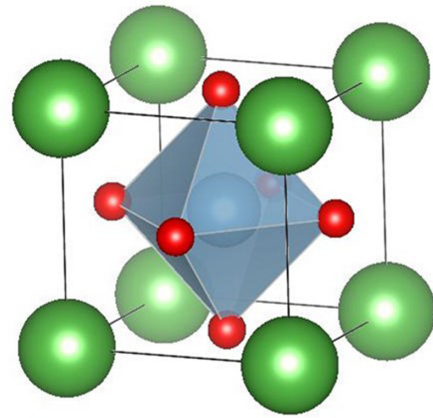


FIG. 2. Hexahedron and octahedron formed by the simple-cubic perovskite structure ABO_3 . The green and red spheres are A and O atoms; the blue sphere at the center is a B atom.

can be described as pseudocubic at room temperature with a lattice constant of 3.790 \AA [26–28]. This value was obtained dividing the room-temperature rhombohedral lattice constant of 5.360 \AA by $\sqrt{2}$. The reported experimental band gap for bulk LAO ranges from 5.6 to 6.5 eV and it has a relatively high dielectric constant ranging from 20 to 27 [29,30]. STO at room temperature has a simple-cubic unit cell with a lattice constant of 3.905 \AA [30]. At about 110 K the structure changes to tetragonal due to a small distortion in the c axis of $c/a = 1.0005$ [28,29]. The reported experimental band gap for STO ranges from 3.25 to 3.41 eV [30,31].

III. STO/LAO SUPERCELL MODELING

The system simulated was an epitaxial thin film of LAO over a substrate of STO, schematically represented in Fig. 3(a). In this model there are two interfaces that dictate the behavior of the heterojunction: the interface of the bulk STO with the LAO thin film and the interface of LAO with vacuum. To simulate the structure of this system, a large supercell containing the interfaces of interest was used [Figs. 3(b) and 3(c)]. The planar dimensions of the supercell were kept as small as possible with just one unit cell, while the height was adjusted to account for the bulk STO and LAO layer of different thickness. The details of the supercell simulation are explained later.

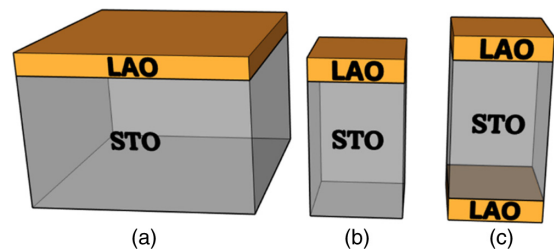


FIG. 3. Schematic representation of the real STO/LAO device (a), nonsymmetric supercell used for the structure optimization (b) and symmetric super cell used for the electronic properties calculations (c).

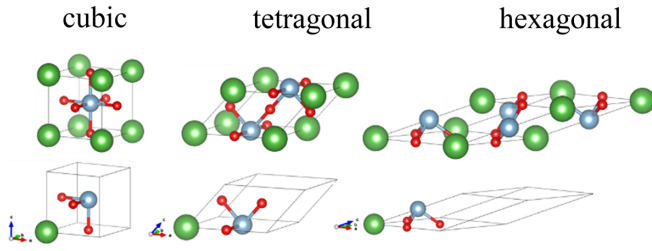


FIG. 4. Primitive representation of the cubic (001), tetragonal (110), and hexagonal (111) perovskite symmetries. The top three structures are the full unit cells and the lower three the translational cells. Green, red, and blue spheres represent A, O, and B atoms, respectively.

The main property analyzed was the emergence of the metallic behavior in the STO/LAO heterojunction in the form of conductivity along the 001, 110, and 111 crystallographic planes. Each plane requires its own crystallographic symmetry description and also all possible surface terminations within one unit cell were accounted. The most intuitive and less complex crystal description for LAO and STO is the simple-cubic perovskite (ABO_3) shown in Fig. 2, which can be directly used to model the 001 interface. The cubic perovskite representation consists of overlay slabs of AO and BO_2 atoms separated by a distance of $\frac{1}{2}$ unit cell. The primitive cell (shown in Fig. 4) has a total of 5 atoms (1 A, 1 B, and 3 O). The Bravais vectors describing the lattice are simple orthonormal; the atoms' positions and Bravais vectors are listed in Table I.

The 110 and 111 unit cells were modeled from the simple cubic, doing a transformation to the Bravais vectors and atomic positions to accommodate the new representations. Here just a brief overview will be presented with emphasis on the STO/LAO system; the general process was explained in detail by Sun and Ceder in Ref. [32]. First the new Bravais vectors (B_1, B_2, B_3) were redefined; note that they are not unique and the newly obtained vectors might not be the ones for the minimal representation. The B_1 and B_2 vectors must be coplanar with the interface or surface needed and the B_3 will be out of plane. To find the plane defined by B_1, B_2 three points are needed, which were calculated from the cubic Bravais vectors and the Miller index of the new plane. Then, calculating the distance between those points, the new Bravais vectors were obtained. For the case of 001 to 110 and 001

to 111 the transformations to the B_1, B_2 vectors are given by Eqs. (1) and (2), respectively:

$$B_2 = A_3 \quad B_1 = \left(\frac{A_2}{k} - \frac{A_1}{h} \right), \quad (1)$$

$$B_2 = \left(\frac{A_3}{l} - \frac{A_1}{h} \right) \quad B_1 = \left(\frac{A_2}{k} - \frac{A_1}{h} \right), \quad (2)$$

where (A_1, A_2, A_3) are the cubic Bravais vectors and (h, k, l) are the new Miller index (110 or 111). Then, the B_3 vector was chosen such that is as small as possible to get closer to the primitive representation; note that it might not be perpendicular to B_1 and B_2 . Now the positions of the atoms must be redefined according to the new set of Bravais vectors. This can be achieved using the covariant transformation defined by Eq. (3):

$$P' = [(O^T)^{-1}P]^T, \quad (3)$$

where P' is a matrix describing the new position of one atom, P is the atom position in the cubic unit cell, and O is the transformation matrix given by $A = OB$ (A and B corresponds to the cubic and new Bravais vectors, respectively). Figure 4 shows the obtained primitive unit cells and Table I shows the corresponding Bravais vectors and atoms positions. The description of the 110 plane resulted in a tetragonal unit cell with overlay slabs of ABO and O_2 . The 111 plane resulted in a hexagonal unit cell with overlay slabs of AO_3 and B. Both 110 and 111 translational cells have the same number of atoms as the 001; the same volume and the overlay slabs are separated by the same factor of $1/2$ times the height of the unit cell.

Given the electronic configuration of LAO, the overlay slabs in all unit cells (cubic, tetragonal, and hexagonal) are polar, where the net excess charge leads to a buildup of electrostatic potential along the A_3 direction. In the 001 plane LAO has a net charge of $(LaO)^{+1}-(AlO_2)^{-1}$, the 110 of $(LaAlO)^{+4}-(O_2)^{-4}$, and the 111 of $(LaO_3)^{-3}-(Al)^{+3}$. In the case of STO the cubic cell is neutral, $(SrO)^{+0}-(TiO_2)^{+0}$, but the tetragonal cell has a net charge of $(SrTiO)^{+4}-(O_2)^{-4}$ and the hexagonal of $(SrO_3)^{-4}-(Ti)^{+4}$. The cubic unit cell has two surface terminations of AO and BO_2 . This implies that the 001 plane has two possible interfaces, between TiO_2/LaO and SrO/AlO_2 . The tetragonal cell has terminations on ABO and O_2 ; therefore, at the 110 plane there will always be an O_2 layer between the overlay slabs. Then just one interface is possible,

TABLE I. Bravais vectors and fractional atom positions for the cubic (001), tetragonal (110), and hexagonal (111) representations of the perovskite structure. The complete equations describing the Bravais vectors of the hexagonal unit cell are shown in the Appendix.

	Cubic			Tetragonal			Hexagonal					
Bravais vectors	A_1	1	0	0	A_1	$\sqrt{2}$	0	0	A_1	a^*	b^*	0
	A_2	0	1	0	A_2	0	1	0	A_2	b^*	a^*	0
	A_3	0	0	1	A_3	$\sqrt{2}/2$	0	$\sqrt{2}/2$	A_3	c^*	c^*	d^*
Atoms fractional positions	A	0	0	0	A	0	0	0	A	0	0	0
	O	1/2	1/2	0	O	1/2	0	0	O	1/2	1/2	0
	O	1/2	0	1/2	O	0	1/2	1/2	O	0	0	0
	O	0	1/2	1/2	O	1/2	1/2	1/2	O	0	1/2	0
	B	1/2	1/2	1/2	B	1/2	1/2	0	B	0	0	1/2

LaAlO₃/O₂/SrTiO₃. The hexagonal cell has two terminations *A*O₃ and *B*; hence, the 111 plane has two interfaces, between LaO₃/Ti and Al/SrO₃.

IV. FIRST-PRINCIPLES CALCULATIONS

Calculations of the electronic and structural properties was done using the formalism of density-functional theory (DFT) [33,34] implemented in the Vienna *Ab initio* Simulation Package (VASP) [35]. The description of the exchange and correlation functionals used was the generalized gradient approximation by Perdew-Burke-Ernzerhof (PBE) [36]. Although the PBE functional is known to severely underestimate the band-gap energy, the density of states (DOS) and energy bands structure obtained are accurate enough to describe the conductive behavior in STO/LAO [36]. PBE gives an accurate description of the interatomic distances, which is of great importance at the simulation of the structure reconstruction of the interface. Also, PBE has the benefit to be not that computationally expensive compared to other functional descriptions. Hybrid (HSE06) and modified Becke-Johnson functionals were tested (shown in Figs. S1 and S2 of the Supplemental Material [37]), yet PBE proves to be the best for this system.

The polar discontinuity was simulated with a dipole correction along the direction perpendicular to the interface. Although interfacial magnetic properties have been reported, spin-polarized calculations were not considered given that none of the atomic species has unpaired electrons. By itself, a regular spin-polarized calculation will not have any effect. The supercell ionic optimization simulates the structural reconstruction of the lattice. A perfectly sharp interface (no La, Sr intermixing) and a perfect lattice with no oxygen vacancies was considered. Scalar relativistic pseudopotentials were used, where the valence electrons are *5s*, *5p*, *4f*, *5d*, *6s* for La (standard); *2s*, *2p* for O (standard); *3s*, *3p* for Al (standard); *4s*, *4p*, *5s* for Sr (Sr_{sv}, semicore *s* states treated as valence), and *3d*, *4s* for Ti (standard). The Brillouin-zone (BZ) sampling was done using the process described by Monkhorst and Pack [38]. Given that in principle the conductive behavior of the systems was unknown, the partial electron occupancies were described using a Gaussian smearing with a sigma value of 0.03 eV. To ensure the insensitivity of the DOS to the electronic smearing, several sigma values were tested, shown in Fig. S3 in the Supplemental Material [37]. For the bulk calculations a convergence study was done, finding that a BZ grid of $5 \times 5 \times 5$ was enough to obtain a converged system. A grid of $5 \times 5 \times 1$ was used for the structure optimization and a denser grid of $7 \times 7 \times 1$ for the DOS calculation. Convergence test of the lattice parameter, energy band gap, and total energy with respect to the energy cutoff value showed that 650 eV is enough to get a precision of 1 mÅ and 1 meV, respectively.

Although there are several possible interfaces depending on the layer where the crystal is cleaved, experimentally the metallic behavior is observed at TiO₂/LaO for 001, SiTiO₂/O₂/LaAlO for 110, and Ti/LaO₃ for 111 planes. For this reason, the results shown will be limited to those interfaces. To keep the stoichiometry of the LAO layers the vacuum surface termination chosen was AlO₂, LaAlO, and

Al for the 001, 110, and 111 planes, respectively. STO surface energy convergence was analyzed to find the thickness needed to decouple the two STO/LAO interfaces in the symmetric supercell. The surface energy calculation followed the procedure described in Ref. [39]. This analysis showed that at 2 unit cells of STO the surface energy difference was smaller than 1 meV. To keep both STO surface terminations symmetric, 3.5 unit cells in thickness was used, shown in Fig. 5. The analysis of the total energy convergence of the systems as function of the vacuum gap thickness showed that above 6 Å the energy difference is on the order of 1 meV. A vacuum gap of 20 Å was used to decouple the two open surfaces. LAO layers with different thickness were evaluated, ranging from 1 to 9 unit cells. To simplify the discussion the results shown will be for LAO layers around the conductive transition presented in the experimental data in Refs. [4,5]. For the 001 plane, just the results from the LAO thickness of 3 and 4 unit cells will be shown. For the 110 plane the results show will be for a LAO thickness of 6 and 7 unit cells, and for 111 plane 8 unit cells. Figure 5 shows the nonoptimized STO/LAO supercells structures for all three planes with a 3-unit-cell LAO layer thickness.

Because of the complexity of the supercell, the structure optimization was performed in several steps until the total energy variation and atomic forces were less than 1.0×10^{-7} eV and 1.0×10^{-3} eV/Å respectively. Due to the computational cost of the ionic minimization for large systems, a smaller nonsymmetrical supercell with just one STO/LAO interface was used to analyze the structural reconstruction (a schematic representation is shown in Fig. 3 and the relaxed structures are shown in Fig. 6). The thickness of the STO and LAO layers in the nonsymmetrical supercell were the same as for the symmetric one. To make the ionic minimization easier the initial in-plane lattice dimensions were set up to those of bulk STO, stretching the LAO layers, and the height positions of the atoms of each material were scaled correctly to match their respective bulk dimension. In addition, the atoms of the lower two layers of STO were fixed, then the system was relaxed, allowing all other atoms, cell volume, and shape to change. Finally, the symmetric LAO/STO/LAO supercell was assembled using the optimized nonsymmetrical cell doing an inversion operation through the central atomic layer in STO to obtain the two LAO/STO/LAO interfaces. The use of a symmetric supercell for the electronic structure calculation is advantageous because it allows further analysis of the stability of the LAO surface at different terminations. For all intended purposes in this paper, the symmetric cell left and right sides have exactly the same properties. Due to this reason, the data presented below are limited to the right side of the symmetric supercell.

V. RESULTS

Three characteristics (structure reconstruction, interface polarization, and charge transfer) of the STO/LAO heterostructure at the 001, 110, and 111 crystallographic planes were analyzed in the calculations, which will be broken into three subsections. The bulk parameters and the optimization of the ions will be discussed in Sec. V A. The effects of the net excess charge in the STO and LAO layers to the intrinsic electric field and the polar discontinuities will be discussed in Sec. V B. Finally, the charge-transfer mechanism and the origin of the metallic behavior are discussed in Sec. V C.

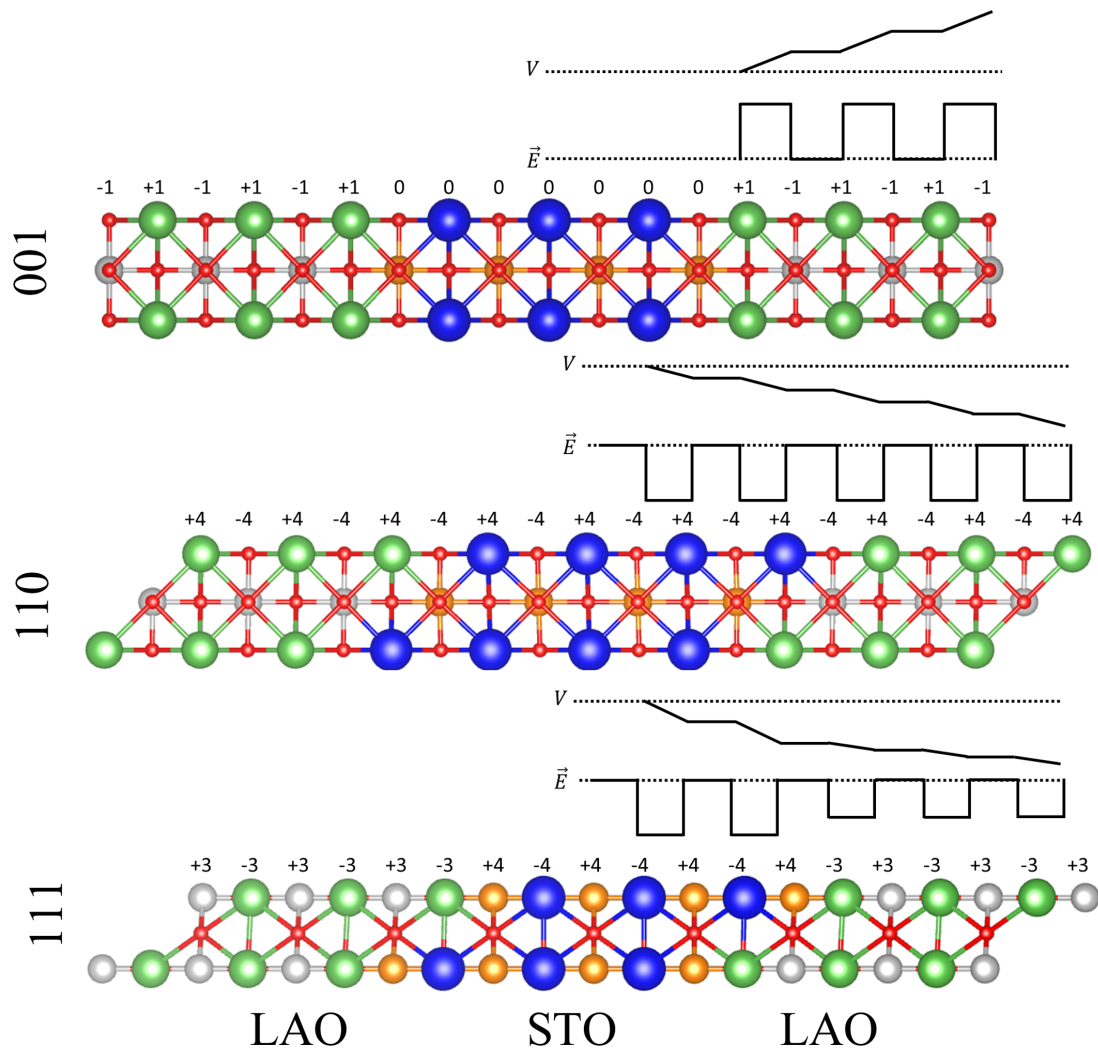


FIG. 5. Symmetric supercells showing the net excess charge of each layer. Based on the ionic model, it represents the intrinsic electric field (\vec{E}) and the electrostatic potential (V). The atomic representation of each sphere is as follows: blue-Sr, orange-Ti, green-La, gray-Al, and red-O.

A. Structure reconstruction

First a conventional bulk calculation was performed to find the optimized lattice dimensions of LAO and STO at the symmetry description of each interface plane (001 cubic, 110 tetragonal, and 111 hexagonal) and ensured that the physical

properties calculated (lattice constant, band gap, etc.) were identical. The ionic configuration of each material was optimized relaxing the cell dimensions. The optimized cubic lattice parameters for bulk STO and LAO obtained were 3.95 and 3.81 Å, respectively, in good agreement with the experimental values (3.905 Å STO and 3.790 Å LAO) and with

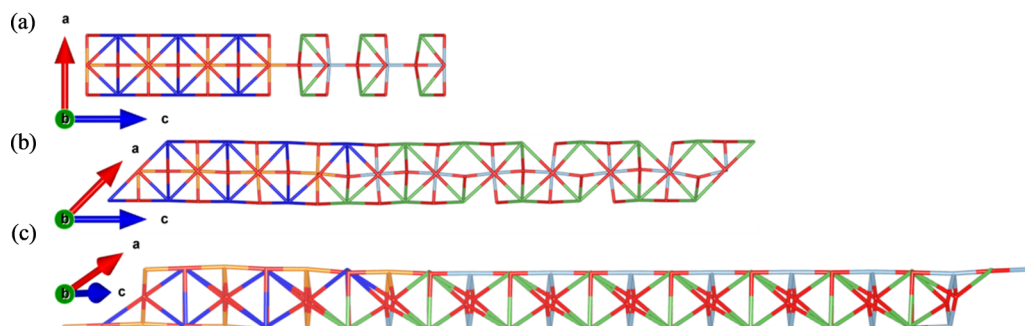


FIG. 6. Structural representation of the optimized STO/LAO structures at (a) 001 (3 LAO layers), (b) 110 (7 LAO layers), and (c) 111 (8 LAO layers) showing the deformation of the lattice. The colors of the bonds are the same as Fig. 5.

previous DFT calculations (3.92 Å STO and 3.84 Å LAO) performed in Refs. [8,9,13,15–17]. As expected, the energy band gaps were underestimated by 38% (3.49 eV) and 49% (1.67 eV) for LAO and STO, respectively, although a wide band-gap insulator was still predicted. The lattice parameter and energy band gap obtained for the tetragonal (STO: 3.9478 Å, 1.671 eV; LAO: 3.8113 Å, 3.517 eV) and hexagonal (STO: 3.9485 Å, 1.678 eV; LAO: 3.8113 Å, 3.624 eV) symmetry was virtually identical to the cubic one with a difference of less than 1%.

The ionic reconstruction of STO/LAO is fairly complex and dependent on the plane of interface the atoms can move in the height (**c**) or planar (**ab**) directions as shown in Fig. 6. The thin layer of LAO is subjected to tensile strain due to STO 2.8% larger mismatch and also to the lattice periodicity disruption at the solid-vacuum interface. The STO layers near the interface are subjected to compressive strain, which rapidly relaxes to almost zero from the second layer on all interfaces. The optimization of the 001 interface resulted in a deformation of the atom positions along the **a** axis, with the **bc** positions remaining unchanged. The relative displacements of the oxygen atoms with respect to the aluminum or titanium in the AlO_2 and TiO_2 layers are the most significant. This produced a bending of the O-Al-O and O-Ti-O bonds along the **a** axis, shown in Fig. 6(a) for 3 LAO layers. For the 110 structure [shown in Fig. 6(b) for 7 LAO layers], the deformations were along the **c** and **a** axis; the **b** positions did not change. In this case the distortion can be visualized as a rotation of the octahedron formed by the oxygen-aluminum and oxygen-titanium atoms. The optimization of the 111 structure resulted in a deformation of the atom positions in the **a**, **b**, and **c** directions [shown in Fig. 6(c) for 8 LAO layers]. The most significant distortion was along the **c** axis, where the oxygen, aluminum, and lanthanum atoms displaced up to 0.40, 0.34, and 0.37 Å, respectively. Increasing the thickness of LAO resulted in a relaxation of its outermost layers (close to the vacuum interface) from the tensile strain at the STO interface on all interfaces. This effect is particularly notable at the 110 and 111 interfaces, where up to 9 LAO layers were used according to the experimental data in Ref. [5].

Although the calculations were performed starting from a LAO layer thickness of 1 unit cell for all planes (001, 110, and 111), the convergence of all systems was not possible. For the 110 and 111 cases the lowest number of LAO layers possible was 5 and 7, respectively. Thinner LAO layers on those planes were very difficult to converge and, in most cases, just failed. This was attributed to the large structure reconstruction on these planes compared to the 001, which might destabilize the LAO layer to the point of disintegration.

B. Interface polarization

The polarity between the STO and LAO depends on the crystallographic plane and the termination layer at the interface between STO/LAO and vacuum. For the 001 plane with STO/LAO interface at $(\text{TiO}_2)^{+0}/(\text{LaO})^{+1}$ and LAO vacuum termination layer in $(\text{AlO}_2)^{-1}$ the discontinuity is from neutral STO to polar LAO (+1, −1) layers, represented in Fig. 5. This produces an electrostatic potential buildup starting from the first LAO layer $[(\text{LaO})^{+1}$ interfacing with $(\text{TiO}_2)^{+0}]$ towards

TABLE II. Intrinsic electric field of the LAO layer and the number of conducting electrons per unit cell.

	LAO layer	001	110	111
Electric field (V/Å)	3	0.178		
	4	0.178		
	6		−0.086	
	7		−0.086	
	8			−0.008
No. electrons/unit cell	3	0		
	4	2.16	2.92	
	6		3.97	
	7		3.77	2.81
	8		2.84	2.87
	9			2.86

the LAO/vacuum interface $(\text{AlO}_2)^{-1}$. In the 110 plane with interface at $(\text{SrTiO})^{+4}/(\text{O}_2)^{-4}/(\text{LaAlO})^{+4}$ and LAO vacuum termination layer in $(\text{LaAlO})^{+4}$ there is no polar discontinuity. The polarity of the layers in both STO and LAO are the same (+4, −4), but there still is a buildup of electrostatic potential in the opposite direction with respect to the 001. For the 111 plane with interface at $(\text{Ti})^{+4}/(\text{LaO}_3)^{-3}$ and LAO vacuum termination layer at $(\text{Al})^{+3}$ the polar discontinuity is between (−4,+4) STO layers to (−3,+3) LAO layers; the buildup of electrostatic potential is in the same direction as the 110 plane.

To analyze the polar behavior, the total electrostatic potential was calculated including the ionic, Hartree, and exchange-correlation contributions. The averaged potential on the **bc** plane as function of the **c** direction was obtained, then further processed to smooth down the fast oscillations between consecutive atomic layers, obtaining the overall buildup of electrostatic potential in the whole system. The smoothing process consists of calculating the average of the electrostatic potential values around some “smoothing radius,” which varies between 20 and 40 data points depending on the frequency of the oscillations. In some cases, the oscillations persisted and more than one smoothing step was performed.

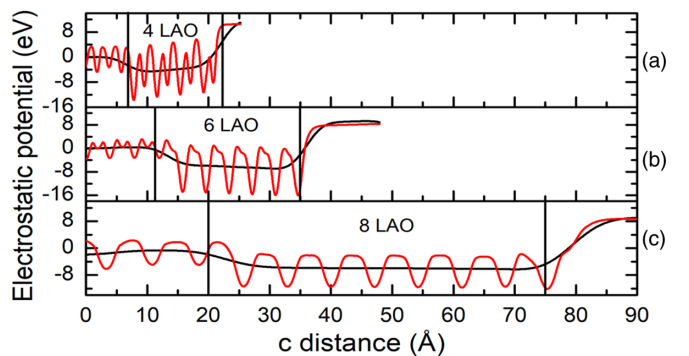


FIG. 7. Average electrostatic potential as function of the **c** position for STO/LAO at the 001 (a), 110 (b), and 111 (c) planes. The red curve is the **ab** plane average potential at each **c** point and the black curve is the result of the smoothing process. The black vertical lines mark the limits of the LAO layer, where at the left the STO layer is located and at the right the vacuum.

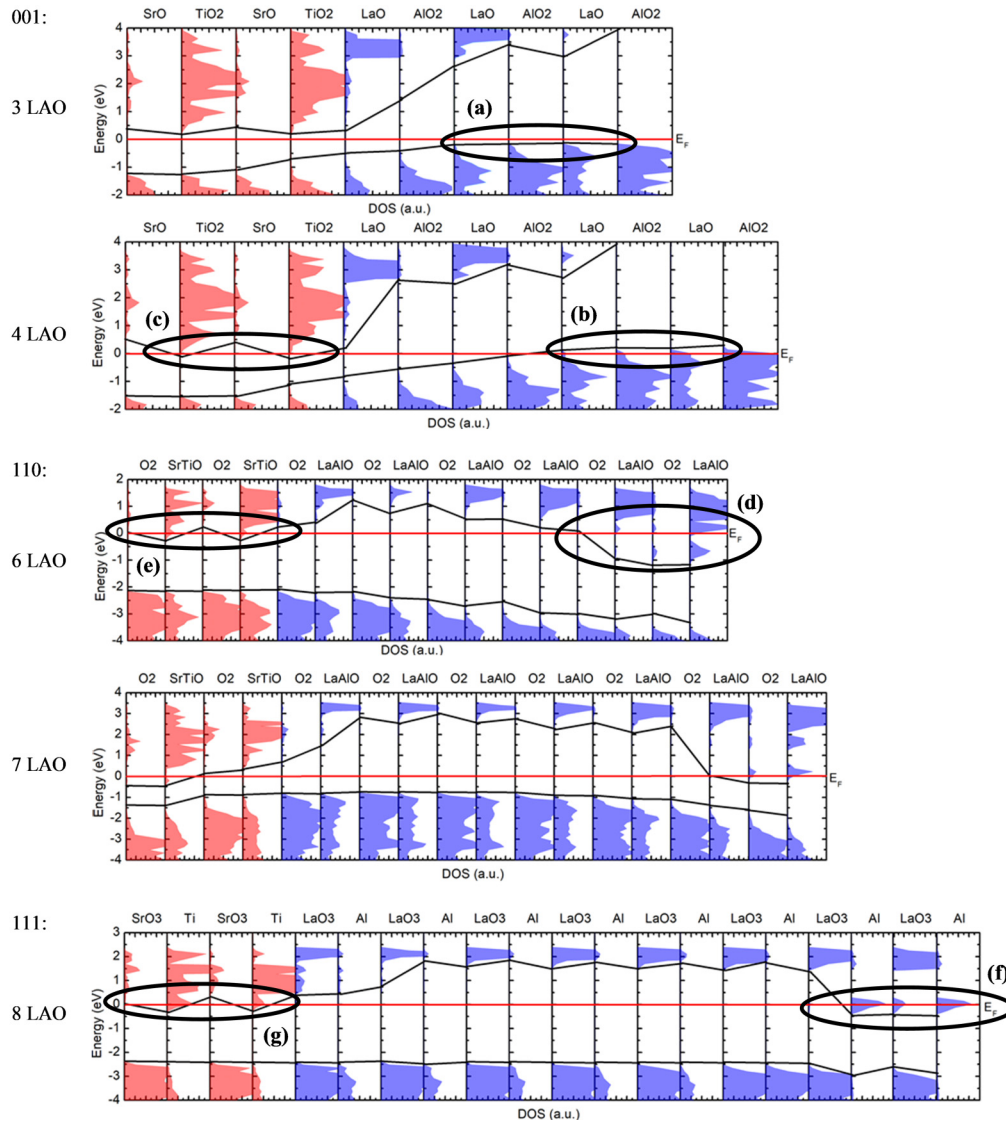


FIG. 8. Layer-projected DOS for STO/LAO at the 001, 110, and 111 planes. The zero at the energy scale corresponds to the Fermi level, also indicated by the red horizontal line. The black stepped line across all STO/LAO layers highlights the changes in the band gap along the interface, representing a detailed energy band diagram of the system. The ellipses (b), (c), (d), (e), (f), and (g) highlight the points where DOS crosses the Fermi energy level.

The smoothed curve is a representation of the average electrostatic potential at the direction perpendicular to the interface as function of position. The slope of this graph between the LAO layers gives an estimate of the average internal electric field, as shown in Table II for all planes. In Fig. 7(a) can be seen the electrostatic potential increasing towards the vacuum layer for the 001 interface with a calculated electric field of 0.178 V/\AA . As expected, in the other two interfaces the electrostatic potential increase negatively towards the vacuum with an electric field of -0.086 and -0.008 V/\AA for the 110 and 111 planes, respectively, shown in Figs. 7(b) and 7(c).

C. Charge transfer

One of the most important tools in understanding how charge carriers behave in complex heterointerfaces is the edge alignment of the valence and conduction states through the

interface. Figure 8 shows the density of states projected for each layer of STO/LAO. Using the well-studied interface at the 001 plane as a benchmark, the shift of the DOS to a higher energy, crossing the Fermi energy in the LAO layers replicates the electronic reconstruction scenario shown in Fig. 1. In Fig. 8(a) it can be appreciated that for the 001 super cell with 3-unit-cell thickness LAO layer there is no DOS crossing the Fermi level, and hence is nonmetallic. For the supercell with 4 unit cells of LAO in thickness, the valence states at the LAO/vacuum interface have been shifted high enough (due to the electrostatic potential buildup) such that the electronic reconstruction happens [Fig. 8(b)]. The electrons tunnel to the nearby available conduction states at the STO/LAO interface [Fig. 8(c)] which are at a distance of 10 to 15 \AA , enabling the 2D conductivity. Integrating the DOS crossing the Fermi level the number of available conducting electrons was calculated to change from 0 to 2.16 electrons per unit cell when the LAO

thickness increased from 3 to 4 unit cells. It is also important to notice that the conduction states are localized at the TiO_2 layers close to the interface.

The 110 and 111 interfaces are very similar but behave differently from 001. The ionic reconstruction of both deforms more the LAO lattice (shown in Fig. 6) and the electrostatic potential buildup is in the opposite direction and in smaller magnitude than the 001 plane. Figures 8(d)–8(g) show the points where the DOS crosses the Fermi energy level, proving their metallic behavior. The main contribution to the conductive states at the 110 plane comes from the LaAlO interfacial with vacuum and the two SrTiO layers close to the STO/LAO interface. The calculated number of conducting electrons (shown in Table II) increases up to a LAO thickness of 6 layers, then it decreases. This is also shown in Fig. 8 for 110 at 7 LAO layers, where the bottom of the conduction band is at a higher energy compared to 6 LAO layers, causing a reduction on the number of DOS crossing the Fermi level. This behavior agrees with Ref. [5], where they reported that the conductivity of STO/LAO at the 110 plane increases to a maximum around a thickness of 6–7 LAO layers and then decreases. The charge accumulation at the 110 interface is partially driven by the shift of the conduction states to lower energies because of the negative buildup of electrostatic potential. The fact that the charge accumulation reaches a maximum could be attributed to the decreasing electron tunneling probability at large distances from the STO layers.

For the 111 plane interface the contribution to the conductive states comes from the last two LAO layers interfacing with vacuum (LaO_3 and O_2) and the first two Ti layers at the STO/LAO interface. The number of available conductive electrons in the 111 plane also increases with thickness for the same reason as the 110 case. A nonconductive to conductive transition was not observed in the 110 and 111 planes; even the 5 and 7 LAO layers showed conductivity (lowest possible number of LAO layers successfully converge for the 110 and 111, respectively). This implies that the electronic reconstruction due to the polar discontinuity is not the main mechanism behind the conductivity in these interfaces. Figure S4 of the Supplemental Material [37] shows a comparison of the DOS for an isolated LAO layer before/after the ionic optimization and the complete STO/LAO. In this figure it can be seen that after ionic optimization the 110 and 111 systems become conductive, whereas the 001 is not (the interface at this plane needs the electrostatic potential buildup of the entire STO/LAO to become conductive). Discarding the chemical intermixing and oxygen vacancies, they were not considered in the supercell models; this makes the structural reconstruction of the mechanism responsible for the conductivity at the 110 and 111 planes.

A further projection of the DOS at the atomic orbitals for the 001 plane (shown in Fig. 9) reveals that the electrons initially come from the p orbitals of the oxygen atoms close to the LAO/vacuum interface and tunnel to the titanium d orbitals close to the STO/LAO interface. For the 110 and 111 planes, shown in Fig. 9, it can be seen that the conductive states come mainly from the titanium d orbitals and the oxygen p orbitals with a small contribution of the aluminum p orbital. The aluminum contribution is smaller than 1 #states/eV and is too small to be seen in Fig. 9.

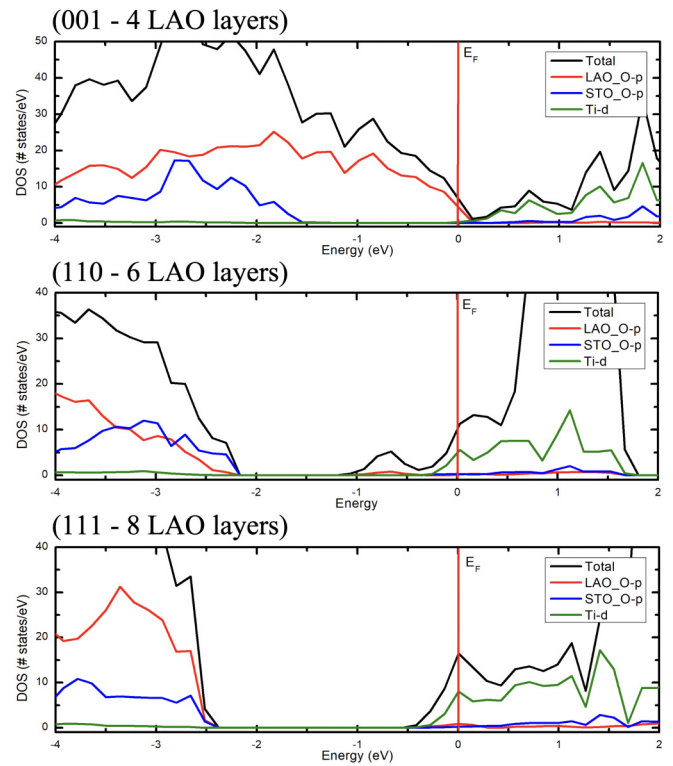


FIG. 9. Projection of the density of states on the atomic orbitals of STO/LAO at the 001 (4 LAO layers), 110 (6 LAO layers), and 111 (8 LAO layers). The black curve represents the total density of states of STO/LAO, red represents the oxygen p projection of the entire LAO layer; blue and green represent the oxygen p and titanium d projections of the entire STO layer.

VI. CONCLUSION

First-principles modeling of the STO/LAO interface at the 001, 110, and 111 crystallographic planes was presented. The emergence of the conductive behavior was analyzed simulating the electronic and structural reconstruction in a LAO/STO/LAO symmetric supercell with LAO layers of different thickness. For the atomically sharp interface with no oxygen vacancies, the emergence of conductivity is the result of charge transfer to the layers close to the interface driven by different mechanism depending on the plane of interface. For the 001 interface the main mechanism behind the conductivity was the polar discontinuity where the electronic reconstruction was found to occur when the LAO layer reached 4 unit cells in thickness undergoing a transition to the conductive state, which is in agreement with other experimental and theoretical studies. The calculated intrinsic electric field was 0.178 V/\AA and the number of conductive electrons was found to increase from 0 to 2.16 electrons per unit cell with a LAO layer thickness of 3 and 4 unit cells, respectively.

For the 110 and 111 interfaces the main mechanism responsible for the conductivity was different from the 001 plane. A transition from a nonconductive to conductive state was not found; the STO/LAO interface was conductive regardless of the thickness of the LAO layer. However, the number of conductive electrons per unit cell was found to increase with the thickness of the LAO layer (up to a certain point in

the 110 system) given a downshift of the DOS caused by the buildup of electrostatic potential, which was in the opposite direction compared to the 001 plane interface. For the 110 interface the number of conductive electrons per unit cell reached a maximum value of 3.97 at a LAO thickness of 6 unit cells, then decreased, in agreement with experimental data. The calculated intrinsic electric field was -0.086 and -0.008 V/Å for the 110 and 111 interfaces, respectively. Given the absence of a critical thickness in the 110 and 111 planes, excluding the chemical intermixing and oxygen vacancies, the main mechanism for the conductivity was attributed to the large structure reconstruction at those interfaces.

ACKNOWLEDGMENTS

D.G.G. gratefully acknowledges the support of the Summer GRA Fellowship supported by the Center for Non-Linear Studies at Los Alamos National Laboratory (LANL) and the LANL/LDRD Program. P.Y. and E.R.B. were funded by the U.S. DOE office of Basic Energy Science under the Heavy Element Chemistry program at LANL. LANL, an affirmative action/equal opportunity employer, is managed

by Triad National Security, LLC, for the National Nuclear Security Administration of the U.S. Department of Energy under Contract No. 89233218CNA000001. The calculations were performed using Environmental Molecular Sciences Laboratory (EMSL) (grid.436923.9), a DOE Office of Science User Facility sponsored by the Office of Biological and Environmental Research at Pacific Northwest National Laboratory.

APPENDIX

Equations describing the Bravais vectors for the hexagonal symmetry of the perovskite structure shown in Table I:

$$a = \frac{\sqrt{2} \times \sqrt{2 + \sqrt{3}}}{2}$$

$$b = \frac{\sqrt{2} \times \sqrt{2 - \sqrt{3}}}{2},$$

$$c = \sqrt{3/2} \times \cos(\tan^{-1}(\sqrt{2}) - \tan^{-1}[\sqrt{2}/2]),$$

$$d = \sqrt{3 - 2 \times c^2}.$$

-
- [1] H. Kroemer, *Int. J. Mod. Phys. B* **16**, 677 (2002).
- [2] N. Nakagawa, H. Y. Hwang, and D. A. Muller, *Nat. Mater.* **5**, 204 (2006).
- [3] M. Kimura, *Jpn. J. Appl. Phys.* **58**, 090503 (2019).
- [4] A. Ohtomo and H. Y. Hwang, *Nature (London)* **427**, 423 (2004).
- [5] G. Herranz, F. Sánchez, N. Dix, M. Scigaj, and J. Fontcuberta, *Sci. Rep.* **2**, 758 (2012).
- [6] B. Kalisky, J. A. Bert, B. B. Klopfer, C. Bell, H. K. Sato, M. Hosoda, Y. Hikita, H. Y. Hwang, and K. A. Moler, *Nat. Commun.* **3**, 922 (2012).
- [7] N. Reyren, S. Thiel, A. D. Caviglia, L. F. Kourkoutis, G. Hammerl, C. Richter, C. W. Schneider, T. Kopp, A.-S. Rüetschi, D. Jaccard, M. Gabay, D. A. Muller, J.-M. Triscone, and J. Mannhart, *Science* **317**, 1196 (2007).
- [8] K. Janicka, J. P. Velev, and E. Y. Tsymbal, *J. Appl. Phys.* **103**, 07B508 (2008).
- [9] S. Davis, Z. Huang, K. Han, Ariando, T. Venkatesan, and V. Chandrasekhar, *Phys. Rev. B* **97**, 041408 (2018).
- [10] A. M. R. V. L. Monteiro, M. Vivek, D. J. Groenendijk, P. Bruneel, I. Leermakers, U. Zeitler, M. Gabay, and A. D. Caviglia, *Phys. Rev. B* **99**, 201102 (2019).
- [11] J. Lee and A. A. Demkov, *Phys. Rev. B* **78**, 193104 (2008).
- [12] F. Schoofs, M. A. Carpenter, M. E. Vickers, M. Egilmez, T. Fix, J. E. Kleibecker, J. L. MacManus-Driscoll, and M. G. Blamire, *J. Phys.: Condens. Matter* **25**, 175005 (2013).
- [13] L. Qiao, T. C. Droubay, V. Shutthanandan, Z. Zhu, P. V. Sushko, and S. A. Chambers, *J. Phys.: Condens. Matter* **22**, 312201 (2010).
- [14] A. Kalabukhov, R. Gunnarsson, J. Börjesson, E. Olsson, T. Claeson, and D. Winkler, *Phys. Rev. B* **75**, 121404 (2007).
- [15] K. Janicka, J. P. Velev, and E. Y. Tsymbal, *Phys. Rev. Lett.* **102**, 106803 (2009).
- [16] A. Chen and Y. Zhi, *J. Appl. Phys.* **71**, 6025 (1992).
- [17] R. Pentcheva and W. E. Pickett, *Phys. Rev. Lett.* **102**, 107602 (2009).
- [18] R. Pentcheva and W. E. Pickett, *Phys. Rev. B* **78**, 205106 (2008).
- [19] L. Guan, F. Tan, G. Shen, Y. Liang, X. Xu, J. Guo, J. Wang, Z. Zhang, and X. Li, *Appl. Surf. Sci.* **475**, 185 (2019).
- [20] A. Annadi, Q. Zhang, X. Renshaw Wang *et al.*, *Nat. Commun.* **4**, 1838 (2013).
- [21] J. I. Beltrán and M. C. Muñoz, *Phys. Rev. B* **95**, 245120 (2017).
- [22] S. A. Hayward, F. D. Morrison, S. A. T. Redfern, E. K. H. Salje, J. F. Scott, K. S. Knight, S. Tarantino, A. M. Glazer, V. Shuvaeva, P. Daniel, M. Zhang, and M. A. Carpenter, *Phys. Rev. B* **72**, 054110 (2005).
- [23] S. Geller and P. M. Raccach, *Phys. Rev. B* **2**, 1167 (1970).
- [24] M. A. Carpenter, S. V. Sinogeikin, and J. D. Bass, *J. Phys.: Condens. Matter* **22**, 035404 (2010).
- [25] S. Lim, J. Kriventsov, S. Haeni, U. Balbashov, F. Reiche, J. L. Freeouf, and G. Lucovsky, *J. Appl. Phys.* **91**, 4500 (2002).
- [26] L. Edge, D. G. Schlom, S. A. Chambers, E. Cicerrella, J. L. Freeouf, B. Holländer, and J. Schubert, *Appl. Phys. Lett.* **84**, 726 (2004).
- [27] M. Schmidbauer, A. Kwasniewski, and J. Schwarzkopf, *Acta Crystallogr., Sect. B* **68**, 8 (2012).
- [28] K. A. Müller, W. Berlinger, and F. Waldner, *Phys. Rev. Lett.* **21**, 814 (1968).
- [29] W. G. Stirling, R. A. Cowley, and A. D. Bruce, *Ferroelectrics* **7**, 401 (1974).
- [30] G. A. Barbosa, R. S. Katiyar, and S. P. S. Porto, *J. Opt. Soc. Am.* **68**, 610 (1978).
- [31] K. Van Benthem, C. Elsässer, and R. H. French, *J. Appl. Phys.* **90**, 6156 (2001).
- [32] W. Sun and G. Ceder, *Surf. Sci.* **617**, 53 (2013).

- [33] R. Nityananda, P. Hohenberg, and W. Kohn, *Resonance* **22**, 809 (2017).
- [34] W. Kohn and L. J. Sham, *Phys. Rev.* **140**, A1133 (1965).
- [35] J. Hafner and G. Kresse, *Properties Complex Inorganic Solids* (Springer, Boston, MA, 1997), Vol. 69.
- [36] J. P. Perdew, K. Burke, and M. Ernzerhof, *Phys. Rev. Lett.* **78**, 1396 (1997).
- [37] See Supplemental Material at <http://link.aps.org/supplemental/10.1103/PhysRevB.104.155306> for a comparison of the DOS calculated with different functionals, the sensitivity of the DOS at different values of the electronic smearing, and the effect of the ionic optimization in the DOS.
- [38] H. J. Monkhorst and J. D. Pack, *Phys. Rev. B* **13**, 5188 (1976).
- [39] V. Fiorentini, *J. Phys.: Condens. Matter* **8**, 6525 (1996).